(1) Cover page

Final Technical Report

Title: Nonvolcanic Tremor and Shear Wave Velocity Structure of the Crust in the Parkfield Region

Authors and Affiliations: Clifford Thurber
University of Wisconsin-Madison
1215 W. Dayton St.
Madison, WI 53706
Phone: (608) 262-6027, FAX: (608) 262-0693
cthurber@wisc.edu

Term Covered by the Award: May 1, 2016 - December 31, 2017

Nonvolcanic Tremor and Shear Wave Velocity Structure of the Crust
in the Parkfield Region

(2) Abstract

We have developed improved three-dimensional (3D) P- and S-wave velocity models and preliminary 3D P- and S-wave attenuation models of the crust in the region surrounding the 2004 Parkfield earthquake rupture. Our effort capitalizes on and extends the work of Thurber et al. (2006), which produced a mid- to upper-crustal 3D P-wave velocity model for this region, and the subsequent work of Zeng et al. (2016) (supported by USGS award G14PA00056), which improved the P-wave model and produced the first good-quality 3D S-wave model for the region. We have further extended our previous work by (a) adding about 10 years of new network P- and S-wave arrival-time data, (b) incorporating P- and S-wave arrival-time data from new stations and temporary arrays, (c) greatly expanding the earthquake S-wave data set by utilizing a new automated S-wave picker on available waveform data, (d) developing surface-wave dispersion data from ambient noise analysis, (e) carrying out a joint inversion of the body- and surface-wave data, and (f) determining preliminary 3D P- and S-wave attenuation models. In addition, (g) we have tested the veracity of the commonly used envelope/station pair differential time method for locating non-volcanic tremor (NVT) by simulating tremor events as the superposition of nearby LFE waveforms (from phase-weighted stacks) and noise, and determining the reliability of the resulting locations. The primary results of our efforts are 3D models for P-wave and S-wave velocity structure for the greater Parkfield area with improved resolution due to the combination of the inclusion of new data and the joint inversion of body- and surface-wave data. We have also produced preliminary P- and S-wave attenuation models. A by-product of the attenuation work is estimates of site response at over 100 seismic stations. These results can be used for waveform modeling studies, crustal deformation analysis using heterogeneous elastic models, and seismic hazard analysis. As in our previous work in other parts of California, our models can provide an effective starting point for future waveform tomography studies. Our work also sheds light on the structure and conditions at the depths where low-frequency earthquakes (LFEs) and non-volcanic tremor (NVT) occur beneath the San Andreas fault (SAF). This is of particular importance considering the possibility that LFEs reflect aseismic slip at depth that may trigger a larger earthquake (Shelly, 2009; Shelly et al., 2009; Shelly, 2015). We find that the envelope/station pair differential time method for locating NVT is subject to severe location bias, such that final locations remain close to the starting locations even when the optimal location is some distance away. This supports the contention that scattered NVT locations beneath the SAF found by some investigators are incorrect, and the true NVT locations more likely coincide with the tightly distributed LFE locations found by Shelly and coworkers. Thus, both LFEs and NVT may indicate the occurrence of aseismic slip at depths below the seismogenic zone that triggers the LFEs and NVT. We infer that the distribution of this slip occurs very close to the vertically downward projection of the SAF, and is not distributed broadly through the lower crust or uppermost mantle.

(3) Main body of the report

Significance of the Project

Our proposed project addresses the following NEHRP goals under Earthquake Physics:

- Develop theory, models, and make field and laboratory measurements of fault zone structure, including damage, permeability, dilatancy, shear localization, alteration, mineralogy, roughness, shear zone width, and evolution of fault structure with accumulated offset and shear strain.

- Conduct field and laboratory studies to ascertain the mechanisms (e.g., fluid flow or fault rheology) responsible for episodic tremor and slip (ETS) as observed in subduction zones, on the San Andreas Fault or in other tectonic settings.

The primary results of our efforts are 3D models for P-wave and S-wave velocity structure for the greater Parkfield area with improved resolution due to the combination of (1) the inclusion of new data and (2) the joint inversion of body- and surface-wave data. We have also produced preliminary P- and S-wave attenuation models. A by-product of the attenuation work is estimates of site response at over 100 seismic stations. These results can be used for waveform modeling studies, crustal deformation analysis using heterogeneous elastic models, and seismic hazard analysis. As in our previous work in other parts of California, our models can provide an effective starting point for future waveform tomography studies. Our work also sheds light on the structure and conditions at the depths where low-frequency earthquakes (LFEs) occur beneath the San Andreas fault (SAF). This is of particular importance considering the possibility that LFEs reflect aseismic slip at depth that may trigger a larger earthquake (Shelly, 2009; Shelly et al., 2009; Shelly, 2015). We find that the envelope/station pair differential time method for locating NVT is subject to severe location bias, such that final locations remain close to the starting locations even when the optimal location is some distance away. This supports the contention that scattered NVT locations beneath the SAF found by some investigators are incorrect, and the true NVT locations more likely coincide with the tightly distributed LFE locations found by Shelly and coworkers. Thus, both LFEs and NVT may indicate the occurrence of aseismic slip at depths below the seismogenic zone that triggers the LFEs and NVT. We infer that the distribution of this slip occurs very close to the vertically downward projection of the SAF, and is not distributed broadly through the lower crust or uppermost mantle.

Background

The completed project directly builds on work that we carried out previously with USGS and Southern California Earthquake Center (SCEC) support. That work is briefly described here to put the new work in context, followed by the details of the completed work.

A substantial effort has been devoted to expanding the P- and S-wave arrival time data set that has been used in our tomographic imaging. The primary source of new S-wave picks came from the application of a new automated picker (Rawles and Thurber, 2015) to three-component permanent network data. This was necessary because very few S-wave picks are available in the network catalogs. We were able to increase the number of network S-wave picks by a factor of nearly 10. The Thurber et al. (2006) Parkfield P-wave study used data only through 2004, so an additional 10 years of network P-wave picks were available. This includes data from a number of PBO stations, which were not installed until after 2004. We also identified a number of quarries for which many explosions have been catalogued by the Northern California network and included them as fixed-location sources in our inversion. Additional data have been obtained from temporary arrays. The principal source of new data is the PERMIT array, deployed in the Cholame area between May 2010 and July 2011 (Horstmann et al., 2013). Earthquake data have also been added from the mini-arrays deployed by Ryberg and co-workers for 6 weeks in 2007 (Shelly et al., 2009; Ryberg et al., 2010).

The most novel data we incorporated were P- and S-wave picks from stacks of LFEs. This is the same type of data as illustrated in Shelly and Hardebeck (2010), but with the addition of many more stations, mainly from temporary arrays, and the use of phase-weighted stacking (PWS) to improve signal-to-noise ratio (Schimmel and Paulssen, 1997; Thurber et al., 2014). We also used cross-correlation of the LFE stacks for nearby families to further improve the pick quality. The addition of these picks from the deep LFE sources combined with deep sampling provided by earthquakes beneath the Coalinga and San Simeon areas yields a resolution of structure in the lower crust in 3D that could not be obtained otherwise. The results from the inversion of the enlarged body-wave data set are described in detail in Zeng et al. (2016).

Research accomplished - joint body wave-surface wave tomography

Many seismic imaging studies have been done for the Parkfield region, at multiple scales. Three-dimensional body-wave tomography studies include Michelini and McEvilly (1991), Eberhart-Phillips and Michael (1993), Thurber et al. (2003; 2004; 2006), Zhang and Thurber (2005), Roecker et al. (2006), Zhang et al. (2009), and Bennington et al. (2013). Several of the small-scale tomography studies that focused on the area around SAFOD produced well-resolved Vp and Vs or Vp and Vp/Vs models, but the large-scale studies of the region lacked sufficient S-wave data to yield Vs or Vp/Vs models. Recently, Zeng et al. (2016) combined data from LFEs and new S-wave picks obtained from an automatic picker (Rawles and Thurber, 2015) to product a Vs model with significantly improved resolution. However, the Vs resolution was still substantially poorer than that for Vp, and the structure of the lower crust remains relatively poorly resolved.

Data from several available permanent networks in this region are used in this study (Figure 1), including the USGS Northern California Seismic Network, the PG&E Central Coast Seismic Network, the Berkeley Digital Seismic Network, and the California Integrated Seismic Network. We also used data from the Plate Boundary Observatory borehole seismic network and the IRIS Transportable Array. Since many stations are equipped with one vertical component, only noise correlation functions (NCFs) between vertical-component pairs have been computed and we used the Rayleigh wave dataset only in this study. We adopted a standard procedure (Bensen et al., 2007) to compute cross-correlation functions of short time windows, then applied the phase-weighted stacking method (Schimmel and Gallart, 2007) to improve signal-to-noise ratio (Zeng and Thurber, 2016).

Figure 1. Map of stations (blue triangles) used for determination of noise correlation functions. The main fault systems are shown by black lines. Large magenta circles denote low-frequency earthquakes. Regular earthquakes are indicated by small dots. Focal mechanisms of moderate-sized events are shown in beach-balls (source: www.globalcmt.org). The dashed green lines indicate positions of model cross-sections AA', BB', CC', and DD' shown in later figures.

4
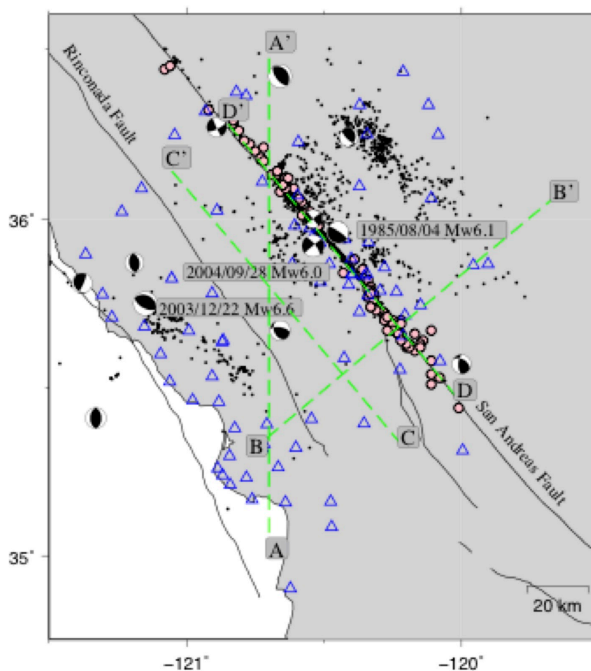
The Rayleigh wave group velocity is automatically measured with an image analysis technique (Yao et al., 2008). 12,990 group velocities are obtained between 1 and 15 s period. The velocity contrast across the SAF has been reported in several body-wave tomography studies (Eberhart-Phillips and Michael, 1993; Thurber et al., 2006; Bennington et al., 2013; Zeng et al., 2016). Figure 2 shows an example group velocity map at a period of 10 s obtained from 2D tomography, demonstrating the presence of the strong velocity contrast across the SAF in the surface-wave data. As Figure 3 shows, group velocity for 5 to 15 s period is sensitive to shear-wave velocity from the near surface to the lower crust. Rayleigh wave group velocity data also provide good constraint on Vp structure at shallow depth (z < 5 km), which is complementary to the earthquake and active source datasets.

The joint inversion of several independent datasets for the same or related physical properties benefits from different sensitivities, which leads to tighter constraints and potentially allows regularization of the inversion to be reduced (Thurber et al., 2016). Therefore, it has been widely used in geophysical imaging, such as joint inversion of receiver function and surface wave dispersion data (Julia et al., 2000), joint inversion of body-wave arrival time and gravity data (Roecker et al., 2004), and joint inversion of seismic and magnetotelluric (MT) data (Bennington et al., 2015). The sensitivities of body and surface waves are complementary to each other and joint inversion of these two datasets has been used on varying scales. Fang et al. (2016) proposed a new direct inversion algorithm, which directly inverts the travel time of the surface wave instead of the traditional two-step inversion scheme, and also avoids the great-circle path assumption. This method has been successfully applied to the southern California region, and has been shown to improve resolution of both Vp and Vs structure and fit seismic waveforms better (Fang et al., 2016). We used this method to jointly invert for 3D Vp and Vs structure with our body-wave arrival time data and Rayleigh wave dispersion measurements obtained from ambient noise.

A key point of joint inversion is how to equalize the constraints from the different datasets. Since both body-wave and surface-wave datasets are expressed as travel times, it is convenient to utilize prior information (e.g. uncertainty) as the relative weight between the two datasets. Our data-driven scheme uses the measurement uncertainty as a relative weight. The uncertainty of the overall body-wave dataset is on the order of 0.03 s, although the uncertainty of S-wave picking is generally larger than that for P-wave picking. The estimated error of the automatic S-wave picker used in our previous study is on the order of 0.1 s, which is very close to the root-mean-square of the residuals (0.099 s) in our tomography result.
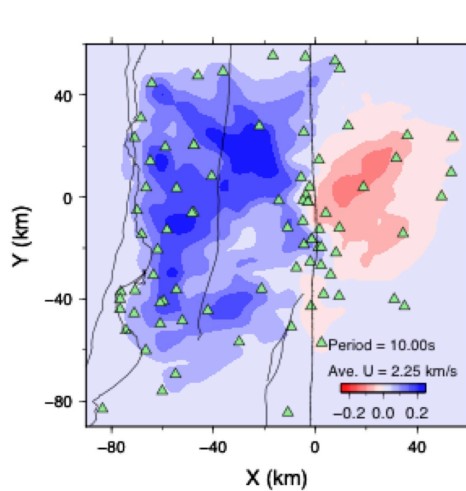

Figure 2. Group velocity map for 10 s Rayleigh waves. The major faults are shown by black lines, with the SAF aligned near X = 0 km. Note the strong velocity contrast across the SAF.
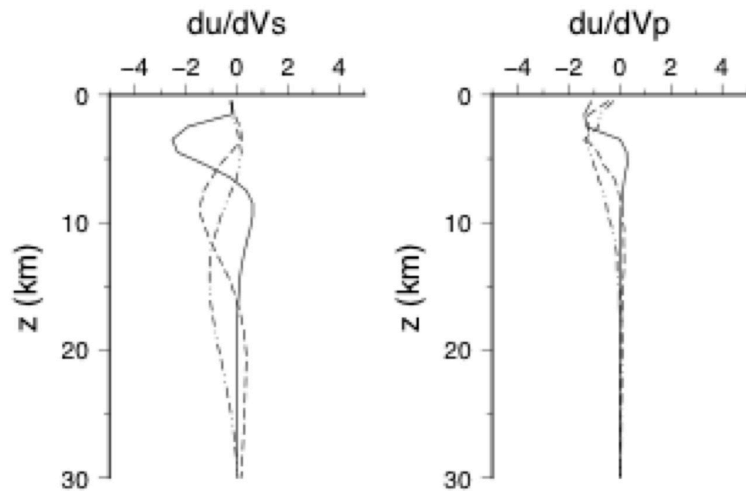
Figure 3. Sensitivity kernels of Rayleigh wave group velocity for 5 s (solid line), 10 s (dashed line), and 15 s (dot-dashed line).

Therefore, 0.1 s is chosen as a conservative estimate of uncertainty for our body-wave dataset. The uncertainty of surface-wave dispersion measurements is more difficult to assess. The standard deviation of a cluster of dispersion curves measured along similar paths has been used as an estimate of uncertainty (Ritzwoller and Levshin, 1998). For large scales (continental/regional), it is on the order of 0.05 km/s (e.g. group velocities of 10-100 s in Ritzwoller and Levshin (1998), phase velocities of 10-30 s in Yao et al. (2006)). But due to the strong heterogeneity in tectonically active regions, this method might be not suitable at a small scale (Bensen et al., 2007). Another approach to estimate the uncertainty of surface-wave dispersion data is the residuals of the inversion (Zhang et al., 2014). A typical value is 1 to several seconds, which also agrees well with a rule-of-thumb estimate (Sabra et al., 2005). Therefore, the weight of body-wave data relative to the surface-wave data should be on the order of 10 based on these approaches.

Another model-driven approach is to seek the optimal relative weight based on the trade-off curve between the misfits of the two datasets (Zhang et al., 2014). The misfit of body-wave and surface-wave data for inversions with different relative weights in a broad range forms the trade-off curve and the optimal relative weight is chosen at the "knee." Figure 4a demonstrates the data-weighting trade-off curve for our dataset. The optimal weight for body-wave data relative to surface-wave data is approximately 10, which is consistent with the value based on the uncertainty estimate. For regularization of the inversion, an L-curve between model roughness and data misfit is obtained and is used to choose the best smoothing factor, yielding an optimal value of 50 (Figure 4b).

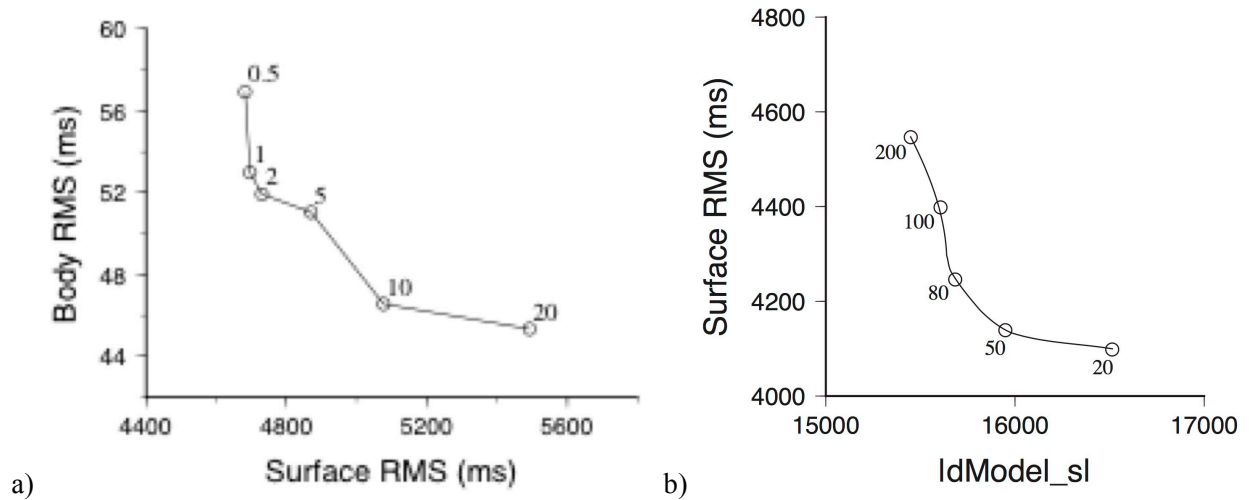a)   b)

Figure 4. (a) Trade-off curve of misfit of body-wave data versus misfit of surface-wave data as a function of the relative data weight. Numbers above the trade-off curve denote the relative weight of body-wave data relative to surface-wave data, with the optimal value chosen as 10. (b) L-curve of misfit of surface-wave data versus norm of the Vs model. Numbers below the L-curve denote the smoothing weight, with the optimal value chosen as 50.

As discussed previously, the complementary nature of the two datasets leads to an expectation of better resolution. The resolution of the joint inversion was evaluated with checkerboard tests. Figure 5 shows the recovery comparison for Vs at 12 km depth, and Figure 6 shows Vs and Vp recovery along profile AA'. First, the paucity of S picks in the body-wave dataset leads to lower resolution of the Vs model in the body-wave only model (Figures 5a, 6a). The sensitivity of the surface wave dispersion data provides additional constraints. As a result, the joint inversion recovers the 0.15° by 0.15° checkers for the Vs model much more successfully than the body waves (Figure 5b). Second, the distribution of earthquakes limits ray coverage at shallow depth and in the lower crust. As the sensitivity kernels show (Figure 3), surface-wave dispersion is also sensitive to Vp in the upper crust in addition to the Vs structure. The recovered checkerboard Vp model supports this claim (Figure 6d and e). The surface-wave

data only inversion recovers the horizontal location of anomalies near the surface, but strong smearing is observed at depth, demonstrating that the structure is strongly blurred in the deeper parts of the model when only surface waves are used (Figure 5c, Figure 6 c and f).
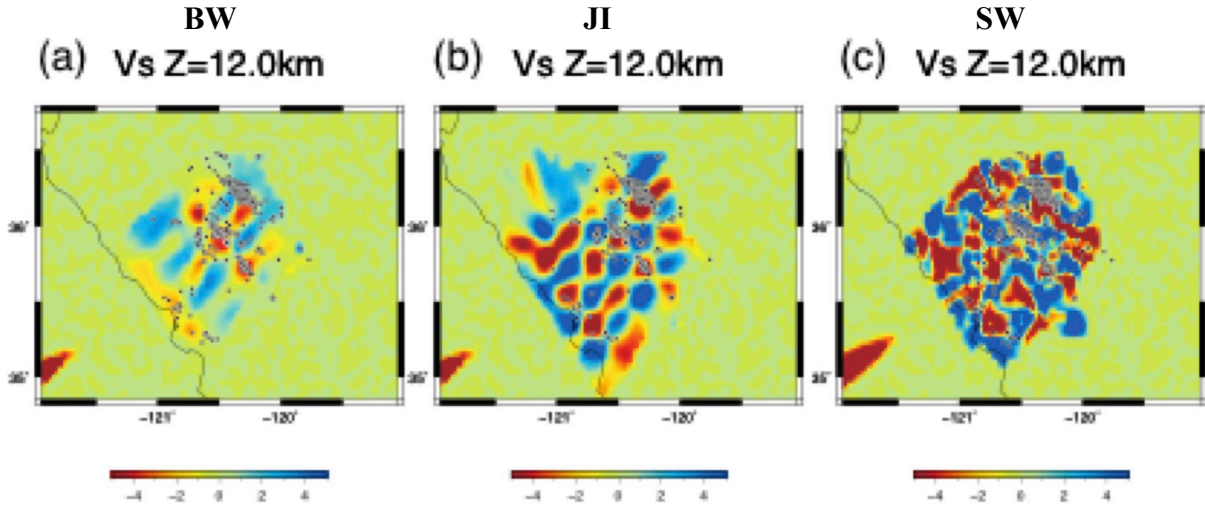

Figure 5. Recovered checkerboard Vs model at a depth of 12 km using different datasets. (a) Body-wave data only, (b) body-wave and surface-wave data (joint inversion), and (c) surface-wave data only. Scale is anomaly in percent.
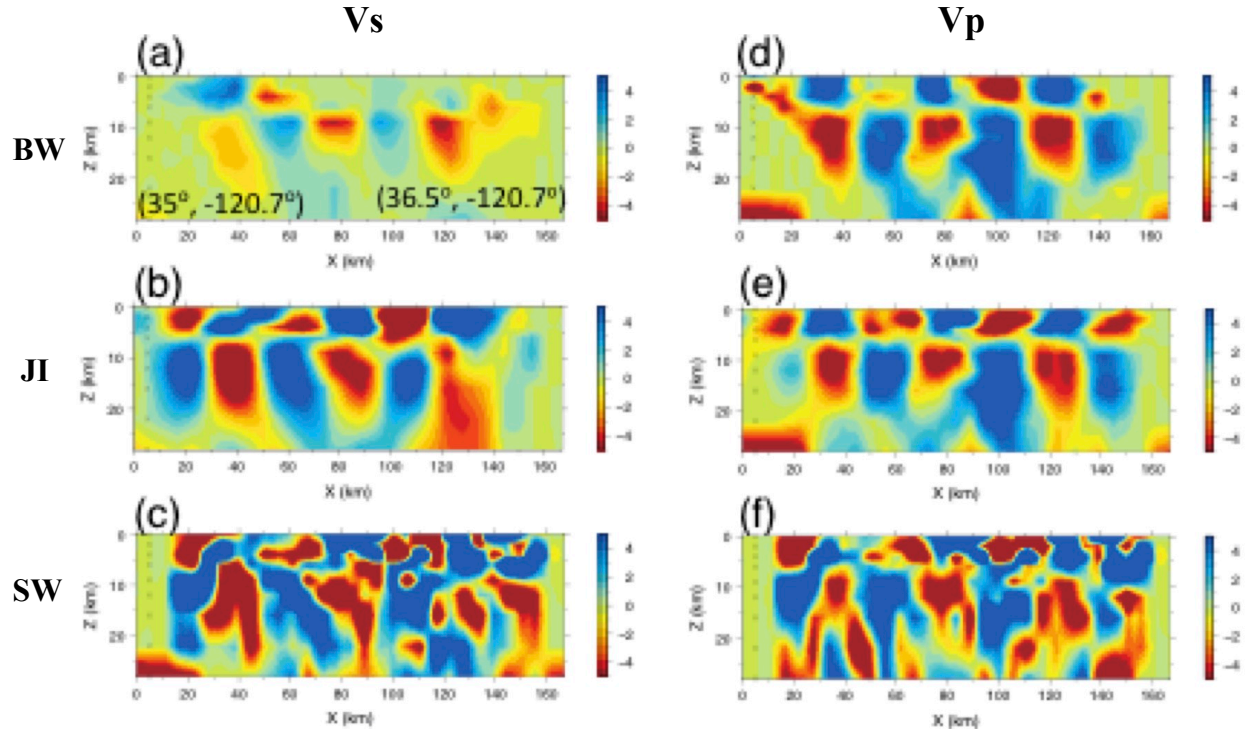

Figure 6. Cross-sections of recovered checkerboard (a-c) Vs and (d-f) Vp models along profile AA' in Figure 1 with different datasets. From top to bottom: body-wave data only (BW), body-wave and surface-wave data (joint inversion, JI), and surface-wave data only (SW). Scale is anomaly in percent.

The spacing of the inversion grid is 0.05° in both latitude and longitude. After inversion, the root-mean-square (RMS) value of the surface-wave data residuals is reduced by 47%, and the RMS of the body-wave data residuals is reduced by 59%. The final Vp and Vs models are shown in Figures 7 and 8, respectively. The structure of the Vp model is generally similar to the previous result (Zeng et al., 2016), but the new Vp model reveals a wide distribution of low-velocity sedimentary rock in the Salinian block between the SAF and Rinconada faults (Figure 7a). An important new feature revealed in our previous Vp model is a low velocity zone in the lower crust, which is consistent with results of MT and refraction studies (Zeng et al., 2016), but this LVZ was not clear in the previous Vs model. Now this LVZ is well imaged in the new Vs model with the surface-wave data (Figure 9). The location of this LVZ is consistent with a zone of strong seismic reflectivity (Trehu and Wheeler, 1987).
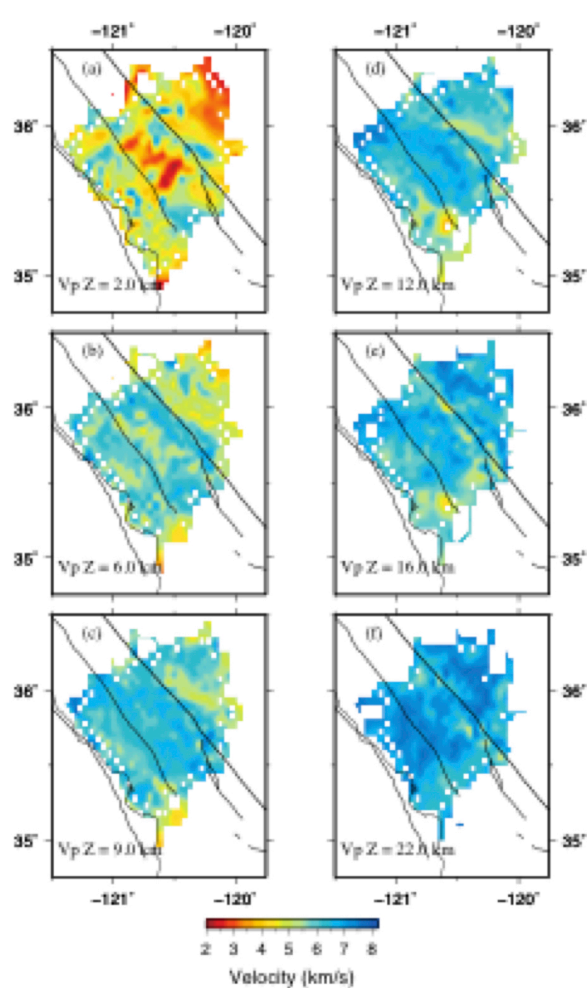

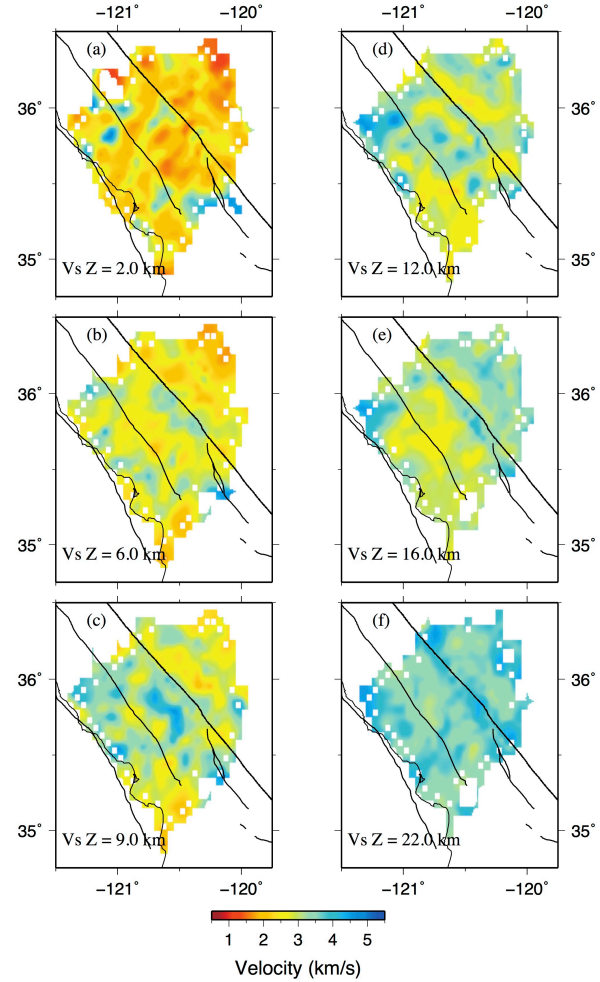Figure 7. Joint inversion Vp model in map views.   Figure 8. Joint inversion Vs model in map views.

In a 2D MT study, a wide high conductivity zone (HCZ) in the lower crust and upper mantle was reported beneath the Salinian block and it was interpreted as a deep fluid source (Becken et al., 2011). Such a high conductivity layer is clearly shown as a low velocity layer in our new Vs model (Figures 8, 9), but the low velocity layer is present only in the crust. This discrepancy can be explained by limitations of the 2D MT inversion scheme. The HCZ in a more recent 3D MT inversion is much smaller and shallower than in the 2D inversion result (Tietze and Ritter, 2013). In the 3D MT inversion result, the HCZ is strongest between 9 and 20 km depth, where the low velocity layer appears in our Vs model.

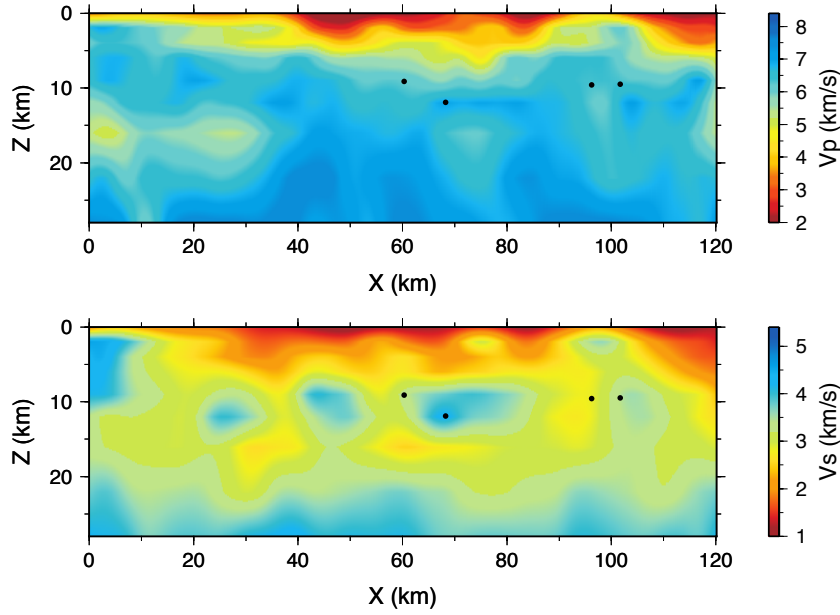A manuscript on these results is in preparation.

Figure 9. Cross-sections through the (top) Vp and (bottom) Vs models along profile CC' in Figure 1, through Salinas Valley. Note the strong low-Vs zones centered around 16 km depth. These low-Vs zones are compatible with the location of a zone of high electrical conductivity in the 3D MT model of Tietze and Ritter (2013).

Research accomplished - preliminary attenuation tomography

We carried out a preliminary study of the 3D attenuation structure of the study region for both P and S waves (i.e., Qp and Qs). Our approach combined the multi-earthquake/multi-station joint inversion for t* and earthquake corner frequencies, low-frequency amplitudes, and site response described in Bisrat et al. (2014) with the tomographic inversions for 3D Qp and Qs structure using the simul2000 code (Thurber and Eberhart-Phillips, 1999). Our dataset consists of approximately 29,000 P-wave t* values and 28,000 S-wave t* values from about 1500 earthquakes observed at a set of over 100 stations. The t* data were fit to about 0.007 s for P and 0.013 s for S. Representative map-view slices through the 3D Qp and Qs models at 6 km depth are shown in Figure 10. The salient features are predominantly high Qp and Qs values on the southwest side of the SAF and much lower Qp and Qs values on the northeast side of the SAF. The lowest Qp and Qs values are found close to the SAF. More data and a comprehensive data quality control analysis are needed to improve model resolution and reduced uncertainties.
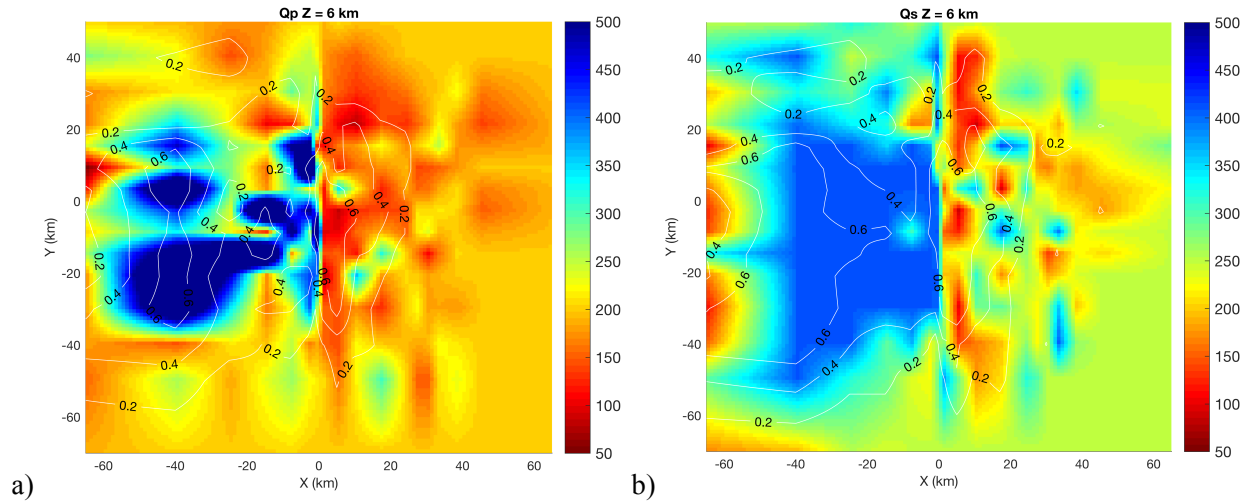

Figure 10. Map-view slices through the preliminary 3D models of (a) Qp and (b) Qs, which are rotated to align the Y axis parallel to the SAF. The SAF runs approximately vertically through the plots close to X = 0 km. The white contours indicate the model diagonal resolution matrix values.

As noted above, the t* inversion procedure also produces individual site response estimates for each station, reflecting the deviation of the average observed spectrum at a given station from the assumed Brune spectral model. Some representative examples for P waves are shown in Figure 11. An effort to validate these site response estimates would be worthwhile. If the site response estimates from the multi-earthquake/multi-station t* inversion can be shown to yield reasonable estimates of the site response determined with another accepted method, then this approach could provide a simple means to develop useful site response estimates anywhere that has enough seismicity to produce a robust t* inversion.
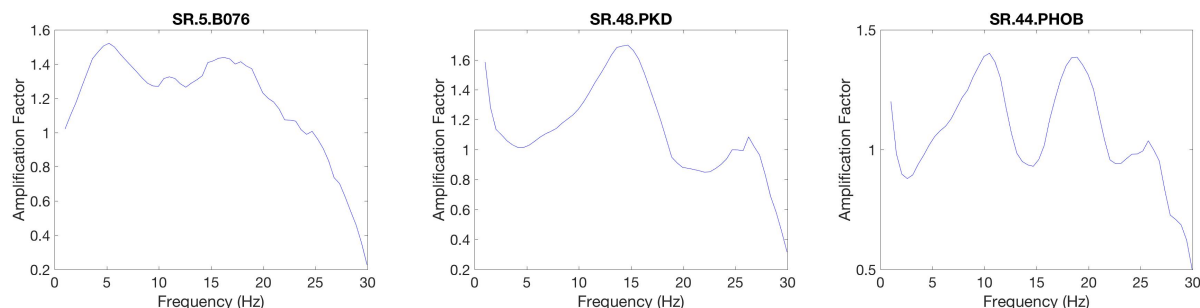

Figure 11. Example site response estimates for three stations, showing some of the variety of responses observed: (left) relatively flat, (center) single amplification peak, (right) two amplification peaks.

Research accomplished - assessment of NVT location accuracy

There has been a long-standing discrepancy between the pattern of NVT locations compared to the pattern of LFE locations along the central SAF. The underlying question is whether or not the scattered locations of SAF NVT in studies such as Nadeau and Dolenc (2005), Nadeau and Guilhem (2009), and Zhang et al. (2010, 2017) are real. Their scattered NVT locations contrast markedly with the tightly clustered LFE locations such as in Shelly and Hardebeck (2010). There is a debate as to whether there is a distinct difference in the sources of NVT versus LFEs, or if instead the scattered NVT locations are due to bias or artifacts in the envelope correlation method used to locate NVT, and NVT and LFEs fundamentally represent the same phenomenon.

We carried out a detailed study to assess how robust and reliable the NVT locations of Nadeau and Dolenc (2005), Nadeau and Guilhem (2009), and Zhang et al. (2010, 2017) actually are. These studies have used differential times from cross-correlation of the envelopes of NVT waveforms, either with a grid search method applied to arrival times differenced from a reference station (Nadeau and Guilhem, 2009) or using a station-pair double-difference (SPDD) method (Zhang et al., 2010, 2017).

We created synthetic tremor event waveforms for use in hypothesis testing. Shelly (pers. comm.) provided us with a comprehensive catalog of LFE detections, identified by LFE family and with precise occurrence times. We took a small sample of NVT events from the catalog of Nadeau (pers. comm.) and determined which LFE families were active during each NVT event and when they occurred during it. We then assembled synthetic NVT waveforms by placing the LFE waveforms, represented by stacks as shown in Thurber et al. (2014), into the synthetic NVT waveform in their time sequence and superimposing noise. This produced synthetic tremor events that closely resemble real NVT events and include LFEs known to have occurred during them. We then processed these synthetic NVT events following the exact methods described in Nadeau and Guilhem (2009).

We next investigated the robustness of the NVT differential time measurements. Consider an NVT event observed at three stations, A, B, and C. Three station-pair differential times, dt, can be formed, dt_{AB}, dt_{BC}, and dt_{AC}. It should be the case that $dt_{AB} + dt_{BC} - dt_{AC} = 0$, but in practice this is not the case, for both real and synthetic NVT data. We term the deviation from zero the "closure error." We hypothesized that closure errors might be responsible for the scattered NVT locations. However, tests with synthetic station-pair differential times with added closure errors, following the statistics of the real NVT data, showed that the effect of the closure errors on the NVT locations was minor. Location errors were typically on the

10

order of a few km, not the tens of km of scattering of the NVT events. In fact, Nadeau and Guilhem (2009) excluded data with large closure errors, so that accounts for the lack of a significant effect, due to the tight statistical distribution of closure errors.

Our second hypothesis was that the SPDD method itself was responsible for the scattered NVT locations of Zhang et al. (2010, 2017). We first experimented with the Equal Differential Time option in the NonLinLoc grid search code (Lomax et al, 2000). We expected to uncover problems related to local minima in the misfit to the data. Unfortunately, we were unable to properly emulate the dynamic residual weighting of the SPDD algorithm with NonLinLoc, so no conclusive results could be obtained. We then performed simple tests on synthetic data with the SPPD algorithm by varying the starting location for a synthetic NVT event along a line connecting the corresponding location in the Nadeau catalog to the centroid of the locations of the LFEs that occurred during the NVT event. The results demonstrated that the SPDD locations are not robust. Rather, the final locations tend to remain very close to the starting locations regardless of how close to or far from the "true" location the starting location is. The problem is also evident for the real data. Figure 12 shows examples of these results.

We conclude that the NVT locations in Zhang et al. (2010, 2017) are very likely biased, because they used the scattered locations from the Nadeau catalog as the starting locations. Further testing of the original Nadeau and Dolenc (2005) and Nadeau and Guilhem (2009) location methods is required to support the inference that NVT locations probably occur in the immediate vicinity of the LFEs, and that NVT and LFEs fundamentally represent the same phenomenon.

These results will form part of the Ph.D. thesis of UW-Madison graduate Bin Guo, and will be submitted for journal publication.
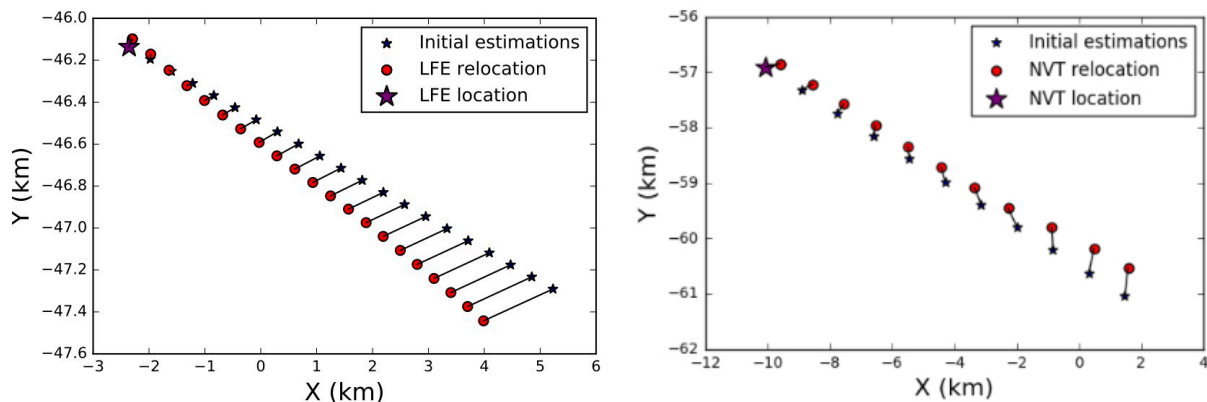

Figure 12. Map views of example of SPDD location applied to (a) a synthetic NVT event for which the true location is the large black star and (b) a real NVT event for which the catalog location is the large black star. The small black stars are the initial locations used as input for the SPDD algorithm. They are connected by lines to the final relocations, the red circles. Note that no matter where the initial location is, the final relocation remains very close to the initial location. Changes in depth show similar patterns.

Conclusions

We have expanded the previously available body-wave arrival time dataset, especially for S waves, analyzed continuous seismic data for extraction of surface-wave dispersion data from ambient noise, and combined the two types of data in a joint inversion for 3D models of Vp and Vs structure of the crust in the region around Parkfield, CA. This effort yields a Vs model with substantially improved resolution compared to previous models. Our results confirm the presence of a low-Vp zone in the lower crust beneath Salinas Valley, and show that a relatively stronger low-Vs zone is also present. The corresponding high Vp/Vs value in this zone supports the presence of fluids, which is consistent with the inference of this being a fluid-rich zone based on the 3D inversion of MT data (Tietze and Ritter, 2013).

Our work on the development of 3D models of Qp and Qs is preliminary in nature, but it does reveal a very strong difference in attenuation on the two sides of the SAF. Q values are generally high southwest of the SAF and generally low northeast of the SAF, with some of the lowest Q values directly along the fault. Our joint inversion for the t* values used to derive the Q models also provides estimates of site response for all of the observing stations. Strong variations in estimated site response are found across the study area. If our site response estimates can be validated for a representative set of stations, then our results will be a significant contribution to site characterization in the region around Parkfield, and could be applied elsewhere.

Our analysis of the SPDD method used to locate NVT (Zhang et al., 2010, 2017) clearly demonstrates the potential for location bias with that method. In tests with synthetic and real NVT data, we find that the final relocations move very little relative to the initial locations, even if the true location of the synthetic event is quite far away. This suggests that the SPDD method suffers from a serious problem with local minima in misfit.

References

Becken, M., Ritter, O., Bedrosian, P. A., and Weckmann, U. (2011), Correlation between deep fluids, tremor and creep along the central San Andreas fault, Nature, 480, 87.

Bennington, N. L., C. Thurber, Z. Peng, H. Zhang, and P. Zhao (2013), Incorporating fault zone head wave and direct wave secondary arrival times into seismic tomography: Application at Parkfield, California, J. Geophys. Res. Solid Earth, 118, 1-7, doi:10.1002/jgrb.50072.

Bennington, N. L., Zhang, H., Thurber, C. H., and Bedrosian, P. A. (2015), Joint inversion of seismic and magnetotelluric data in the Parkfield region of California using the normalized cross-gradient constraint, Pure Appl. Geophys., 172, 1033-1052.

Bensen, G. D., Ritzwoller, M. H., Barmin, M. P., Levshin, A. L., Lin, F., Moschetti, M. P., and Yang, Y. (2007), Processing seismic ambient noise data to obtain reliable broad-band surface wave dispersion measurements, Geophys. J. Int., 169, 1239-1260.

Bisrat, S. T., H. R. DeShon, J. Pesicek, and C. Thurber (2014), High-resolution 3-D P wave attenuation structure of the New Madrid Seismic Zone using local earthquake tomography, J. Geophys. Res. Solid Earth, 119, 409-424, doi:10.1002/2013JB010555.

Eberhart-Phillips, D., and Michael, A. J. (1993), Three-dimensional velocity structure, seismicity, and fault structure in the Parkfield region, central California, J. Geophys. Res., 98, 15737-15758.

Fang, H., Zhang, H., Yao, H., Allam, A., Zigone, D., Ben-Zion, Y., Thurber, C. and van der Hilst, R. D. (2016), A new algorithm for three-dimensional joint inversion of body wave and surface wave data and its application to the Southern California plate boundary region, J. Geophys. Res. Solid Earth, 121, 3557-3569.

Horstmann, T., R. M. Harrington, and E. S. Cochran (2013), Semi-automated tremor detection using a combined cross-correlation and neural network approach, J. Geophys. Res., 118, 1-20, B50345.

Julia, J., C. J. Ammon, R. B. Herrmann, and A. M. Correig (2000), Joint inversion of receiver function and surface wave dispersion observations, Geophys. J. Int., 143, 99-112.

Lomax, A., J. Virieux, P. Volant and C. Berge (2000), Probabilistic earthquake location in 3D and layered models: Introduction of a Metropolis-Gibbs method and comparison with linear locations, in Advances in Seismic Event Location, C. H. Thurber, and N. Rabinowitz (eds.), Kluwer, Amsterdam, pp. 101-134.

Michelini, A., and T.V. McEvilly (1991), Seismological studies at Parkfield: I, Simultaneous inversion for velocity structure and hypocenters using cubic B-splines parameterization, Bull. Seism. Soc. Am. 81, 524-552.

Nadeau, R., and Dolenc, D. (2005), Novolcanic tremors deep beneath the San Andreas Fault, Science, 307, 389-389.

Nadeau, R. M., and A. Guilhem, (2009), Nonvolcanic tremor evolution and the San Simeon and Parkfield, California, earthquakes, Science, 325, 191-193.

Rawles, C., and C. Thurber (2015), A nonparametric method for automatic determination of P-wave and S-wave arrival times: Application to local microearthquakes, Geophys. J. Int., 202,1164-1179, doi:10.1093/gji/ggv218.

Ritzwoller, M. H., and Levshin, A. L. (1998), Eurasian surface wave tomography: Group velocities, J. Geophys. Res.: Solid Earth, 103, 4839-4878.

Roecker, S., Thurber, C., and McPhee, D. (2004), Joint inversion of gravity and arrival time data from Parkfield: New constraints on structure and hypocenter locations near the SAFOD drill site, Geophys. Res. Lett., 31, L12S04.

Ryberg, T., C. Harberland, G. S. Fuis, W. L. Ellsworth, and D. R. Shelly (2010), Locating non-volcanic tremor along the San Andreas Fault using a multiple array source imaging technique, Geophys. J. Int., 183, 1485-1500.

Sabra, K. G., Gerstoft, P. Roux, P., Kuperman, W. A. and Fehler, M. C., (2005), Surface wave tomography from microseisms in Southern California, Geophys. Res. Lett., 32, L14311, doi:10.1029/2005GL023155.

Schimmel, M., and J. Gallart (2007), Frequency-dependent phase coherence for noise suppression in seismic array data, J. Geophys. Res., 112, B04303, doi:10.1029/2006JB004680.

Schimmel, M. and H. Paulssen (1997), Noise reduction and detection of weak, coherent signals through phase-weighted stacks, Geophys. J. Int., 130, 497-505, doi: 10.1111/j.1365-246X.1997.tb05664.x.

Shapiro, N. M., Campillo, M., Stehly, L., and Ritzwoller, M. H. (2005), High-resolution surface-wave tomography from ambient seismic noise, Science, 307, 1615-1618.

Shelly, D. R. (2009), Possible deep fault slip preceding the 2004 Parkfield earthquake, inferred from detailed observations of tectonic tremor, Geophys. Res. Lett., 36, L17318, doi:10.1029/ 2009GL039589.

Shelly, D. R. (2015), Complexity of the deep San Andreas Fault zone defined by cascading tremor, Nature Geosci., doi:10/1038/ngeo2335.

Shelly, D. R., Ellsworth, W. L., Ryberg, T., Haberland, C., Fuis, G. S., Murphy, J., Nadeau, R. and Bürgmann, R. (2009), Precise location of San Andreas fault tremors near Cholame, California using seismometer clusters: Slip on the deep extension of the fault?, Geophys. Res. Letts., 36, L01303.

Shelly, D. R., and J. L. Hardebeck (2010), Precise tremor source locations and amplitude variations along the lower-crustal central San Andreas Fault, Geophys. Res. Lett., 37, L14301, doi:10.1029/2010GL043672.

Thurber, C. H., N. Bennington, H. Zhang, H. Fang, M. Maceira, X. Zeng, and A. Allam (2016), Methods and applications of joint geophysical inversion, Integrated Imaging of the Earth Workshop, London.

Thurber, C., S. Roecker, K. Roberts, M. Gold, L. Powell, and K. Rittger (2003), Earthquake locations and three-dimensional fault zone structure along the creeping section of the San Andreas Fault near Parkfield, CA: preparing for SAFOD, Geophys. Res. Lett., 30, 10.1029/2002GL016004.

Thurber, C., S. Roecker, H. Zhang, S. Baher, and W. Ellsworth (2004), Fine-scale structure of the San Andreas fault and location of the SAFOD target earthquakes, Geophys. Res. Lett., 31, L12S02, doi: 10.1029/2003GL019398.

Thurber, C., X. Zeng, A. Thomas, and P. Audet (2014), Phase-weighted stacking applied to low-frequency earthquakes, Bull. Seism. Soc. Am., 104, doi:10.1785/0120140077.

Thurber, C., Zhang, H., Waldhauser, F., Hardebeck, J., Michael, A., and Eberhart-Phillips, D. (2006), Three-dimensional compressional wavespeed model, earthquake relocations, and focal mechanisms for the Parkfield, California, region, Bull. Seismol. Soc. Am., 96, S38-S49.

Tietze, K., and Ritter, O. (2013), Three-dimensional magnetotelluric inversion in practice - the electrical conductivity structure of the San Andreas Fault in Central California, Geophys. J. Int., 195, 130-147.

Trehu, A. M., and Wheeler, W. H. (1987), Possible evidence for subducted sedimentary materials beneath central California, Geology, 15, 254-258.

Yao, H., van Der Hilst, R. D., and De Hoop, M. V. (2006), Surface-wave array tomography in SE Tibet from ambient seismic noise and two-station analysis - I. Phase velocity maps, Geophys. J. Int., 166, 732-744.

Yao, H., Beghein, C., and van der Hilst, R. D. (2008), Surface wave array tomography in SE Tibet from ambient seismic noise and two-station analysis - II. Crustal and upper-mantle structure, Geophys. J. Int., 173, 205-219.

Zeng, X., and Thurber, C. H. (2016), A Graphics Processing Unit implementation for time–frequency phase-weighted stacking, Seism. Res. Lett., 87, 358-362.

Zeng, X., Thurber, C. H., Shelly, D. R., Harrington, R. M., Cochran, E. S., Bennington, N. L., Peterson, D., Guo, B. and McClement, K. (2016), 3-D P-and S-wave velocity structure and low-frequency earthquake locations in the Parkfield, California region, Geophys. J. Int., 206, 1574-1585.

Zhang et al. (2010)

Zhang, H., Maceira, M., Roux, P., and Thurber, C. (2014), Joint inversion of body-wave arrival times and surface-wave dispersion for three-dimensional seismic structure around SAFOD, Pure App. Geophys., 171, 3013-3022.

Zhang, H., and C. Thurber (2005), Adaptive mesh seismic tomography based on tetrahedral and Voronoi diagrams: Application to Parkfield, California, J. Geophys. Res. Solid Earth, 110, B04303, doi: 10.1029/2004JB003186.

Zhang, H., Thurber, C., and Bedrosian, P. (2009), Joint inversion for Vp, Vs, and Vp/Vs at SAFOD, Parkfield, California, Geochem., Geophys., Geosys., 10, Q11002.

Zhang, H., Nadeau, R., and Guo, H. (2017), Imaging the nonvolcanic tremor zone beneath the San Andreas fault at Cholame, California using station-pair double-difference tomography, Earth Planet. Sci. Lett., 460, 76-85.

(4) Bibliography

Thurber, C. H., N. Bennington, H. Zhang, H. Fang, M. Maceira, X. Zeng, and A. Allam (2016), Methods and applications of joint geophysical inversion, Integrated Imaging of the Earth Workshop, London, UK.

Thurber, C. H., A. Nayak, H. Fang, and H. Zhang (2018), Tomographic imaging of the Central California crust with multiple methods, 2018 SSA-LACSC Conference, Miami, FL.